



Article

Concentration Optimization of Localized Cu^0 and Cu^+ on Cu-Based Electrodes for Improving Electrochemical Generation of Ethanol from Carbon Dioxide

Hong Lu ¹, Guan Wang ¹, Yong Zhou ¹, Aselefech Sorsa Wotango ², Jiahao Wu ³, Qi Meng ³ and Ping Li ^{1,*}

¹ School of Flexible Electronics (SoFE) & Institution of Advanced Materials (IAM), Nanjing Tech University, 30 South Puzhu Road, Nanjing 211816, China

² Center of Excellence in Sustainable Energy, Department of Industrial Chemistry, Addis Ababa Science and Technology University, Amist Kilo, Addis Ababa 16417, Ethiopia

³ School of Physical and Mathematical Sciences, Nanjing Tech University, 30 South Puzhu Road, Nanjing 211816, China

* Correspondence: iampingli@njtech.edu.cn; Tel.: +86-18260086256

Abstract: Copper-based electrodes can catalyze electroreduction of CO_2 to two-carbon products. However, obtaining a specific product with high efficiency depends on the oxidation state of Cu for the Cu-based materials. In this study, Cu-based electrodes were prepared on fluorinated tin oxide (FTO) using the one-step electrodeposition method. These electrodes were used as efficient electrocatalysts for CO_2 reduction to ethanol. The concentration ratio of Cu^0 and Cu^+ on the electrodes was precisely modulated by adding monoethanolamine (MEA). The results of spectroscopic characterization showed that the concentration ratio of localized Cu^+ and Cu^0 (Cu^+/Cu^0) on the Cu-based electrodes was controlled from 1.24/1 to 1.54/1 by regulating the amount of MEA. It was found that the electrode exhibited the best electrochemical efficiency and ethanol production in the CO_2 reduction reaction at the optimal concentration ratio Cu^+/Cu^0 of 1.42/1. The maximum faradaic efficiencies of ethanol and C_2 were 48% and 77%, respectively, at the potential of -0.6 V vs. a reversible hydrogen electrode (RHE). Furthermore, the optimal concentration ratio of Cu^+/Cu^0 achieved the balance between Cu^+ and Cu^0 with the most favorable free energy for the formation of $^*\text{CO}$ intermediate. The stable existence of the $^*\text{CO}$ intermediate significantly contributed to the formation of the C–C bond for ethanol production.

Keywords: electrochemical CO_2 reduction; Cu-based electrode; ethanol production; valence state regulation



Citation: Lu, H.; Wang, G.; Zhou, Y.; Wotango, A.S.; Wu, J.; Meng, Q.; Li, P. Concentration Optimization of Localized Cu^0 and Cu^+ on Cu-Based Electrodes for Improving Electrochemical Generation of Ethanol from Carbon Dioxide. *Int. J. Mol. Sci.* **2022**, *23*, 9373. <https://doi.org/10.3390/ijms23169373>

Academic Editor: Sun-Jae Kim

Received: 11 August 2022

Accepted: 18 August 2022

Published: 19 August 2022

Publisher's Note: MDPI stays neutral with regard to jurisdictional claims in published maps and institutional affiliations.



Copyright: © 2022 by the authors. Licensee MDPI, Basel, Switzerland. This article is an open access article distributed under the terms and conditions of the Creative Commons Attribution (CC BY) license (<https://creativecommons.org/licenses/by/4.0/>).

1. Introduction

An electrochemical CO_2 reduction reaction (CO_2RR) uses electrical energy to convert CO_2 molecules into hydrocarbon products, which can store the intermediate electricity as chemical energy in the form of fuels [1]. Various products, such as carbon monoxide [2–4], formic acid [5,6], methane [7], methanol [8], ethylene [9,10], acetic acid [11], ethanol [12,13], and minor C_3+ products [14], have been acquired from direct and homogeneously catalyzed CO_2 reduction. The selectivity of a specific product of the CO_2RR is heavily dependent on the electrocatalysts. Generally, Zn [4], Ag [2], and Pd [3] metals are extensively explored to produce CO, while Sn [5], Bi [5], and Pb [6] metals have been studied to generate HCOOH from the CO_2RR . Other high-value products containing alcohols and olefins are difficult to obtain from the CO_2RR owing to their multi-electron requirement, which is provided by the surface atomic arrangement of electrocatalysts. A significant barrier to this conversion is the lack of efficient and robust catalysts for CO_2 reduction, particularly the catalysts that can realize high-order products such as ethanol, methanol, or multi-carbon compounds.

Among conventional electrocatalysts, Cu-based electrodes can effectively enhance CO_2 conversion into two-carbon products, such as ethanol and ethylene, owing to their

unique electron energy density [15,16]. Simultaneously, the appropriate binding energy between the Cu electrode and intermediate *CO can stabilize protonated intermediates to inhibit the CO gas generation, which would poison the electrode [17]. For the CO₂RR, Cu-based electrodes have higher selectivity to ethylene than ethanol owing to its lower energy barrier [18]. This implies that for Cu-based electrocatalysts with different reaction intermediates, ethanol production requires strict thermodynamic and dynamic conditions [19]. Correspondingly, the specific intermediate generated during the reaction determines the final products [20,21]. For example, *CO is generally considered to be the common initial intermediate for products such as alkanes and alcohols. An appropriate amount of adsorbed *CO species can be dimerized to CO–CO, which is the key intermediate for C–C coupling and C₂ products formation, e.g., *C₂H_xO (x = 0–4) compounds [22]. Sufficient amounts of *CO on the surface of the electrocatalyst shortens the distance of C–C coupling, effectively improving the generation of two-carbon compounds. Moreover, the abundant *CO distribution is beneficial for protonation, helping to produce ethanol by lowering the energy barrier of ethanol formation [23]. For Cu-based electrodes, fine-tuning the electrode interface provides an opportunity to improve C–C coupling for the desired product. In particular, Cu-based materials with mixed valence states of Cu are advantageous for the C–C coupling in obtaining two-carbon products [24]. This is because mixed valence states form partial positively (*CO–Cu⁺) and partial negatively charged (*CO–Cu⁰) carbons, which result in the C–C coupling through electrostatic interaction. Cu⁰ undergoes chemical adsorption with the curved structure of CO₂ owing to its full-shell electronic structure, and carbon atoms becomes negatively charged. At the same time, Cu⁺ combines H₂O molecules with CO₂ to form a hydrogen bond; the negative charge accumulates on the O atoms of CO₂; the carbon atoms become positively charged [25]. The carbon atoms of two *CO on the Cu⁺ and Cu⁰ regions are positively and negatively charged, respectively, facilitating the C–C coupling. Shang et al. prepared a core–shell Cu catalyst (Cu@Cu₂O), that is, a thin layer of Cu₂O on the Cu surface, under environmental conditions. The synergistic effect between Cu⁺ and Cu⁰ on Cu@Cu₂O increases ethanol yield and selectivity with faraday efficiency (FE) of 29% [26]. To produce ethanol efficiently, some researchers have also combined Cu compounds with other metal and semiconductor materials on the electrode interface. Cu@VO₂ [27] and Au_x/Cu₂O [28] electrocatalysts were skillfully designed for ethanol generation, and their catalytic mechanisms were proposed. Molecular CO generated on Au or VO₂ shifts to the adjacent Cu element, reducing the free energy of *COCO formation. Additionally, Cu plays an important role in the CO₂RR. The correlation between ethanol production and the valence state of Cu should be urgently explored to enhance the CO₂RR using a simple and effective approach.

In this study, Cu-based electrodes were prepared on fluorinated tin oxide (FTO) using the one-step electrodeposition method. Moreover, these electrodes were used as efficient electrocatalysts for CO₂ reduction to ethanol. Monoethanolamine (MEA)—a complexing agent of the precursor Cu²⁺ ions—was used in the preparation process. The results showed that adding MEA precisely modulated the concentration ratio of Cu⁰ and Cu⁺ on the electrodes. This can probably be attributed to the complex formation between MEA and Cu²⁺ ions ([Cu(MEA)₂]²⁺) in the precursor solution. On the one hand, the strong bonding effect between Cu²⁺ and MEA restrained the reduction of Cu²⁺ ions on the electrode. Likewise, the existence of [Cu(MEA)₂]²⁺ inhibited the movement of Cu²⁺ ions to the electrode owing to its larger relative atomic mass than Cu²⁺ ions. These two factors simultaneously inhibited the reduction of Cu²⁺ ions and extended the existence time of Cu⁺ ions on the electrode. The spectroscopy characterization demonstrated that the concentration ratio of Cu⁺ and Cu⁰ on the Cu-based electrodes was controlled from 1.24/1 to 1.54/1 by regulating the amount of MEA. Moreover, the Cu-based electrodes prepared using MEA also significantly improved ethanol production, particularly at a lower voltage. For the Cu-based electrode containing the MEA volume ratio of 0.6% (Cu_{0.6}), the maximum FE of ethanol was 48% and C₂ was 77% at –0.6 V vs. RHE. The concentration ratio of Cu⁺/Cu⁰ was 1.42/1 for Cu_{0.6}, and the electrode probably achieved the balance

between Cu^+ and Cu^0 with a stabilized $^*\text{CO}$ intermediate. The abundant $^*\text{CO}$ intermediates contributed to the formation of the C–C bond for ethanol production.

2. Results and Discussion

2.1. Morphology of Cu-Based Electrodes

The Cu-based electrodes were prepared using copper nitrate and MEA as the reaction precursor, and the morphology and valence state agent, respectively, by constant potential electrodeposition at room temperature. In particular, $\text{Cu}_{0.6}$ and $\text{Cu}_{1.2}$ electrodes were obtained by adding MEA with a volume ratio of 0.6% and 1.2% to 0.1 mol/L copper nitrate, respectively. For comparison, a Cu-based electrode was fabricated without MEA using the same electrodeposition parameters (denoted as Cu_0). Scanning electron microscopy (SEM) images showed that microparticles monodisperse on the electrode in isolation with a size of approximately 2 μm , and Cu_0 consisted of several small nanoparticles with a diameter of 100 nm (Figures 1a and 2c–f). These microparticles were grown on the Cu-based materials formed on the conductive layer of FTO (Figure 2a,b). In comparison, the $\text{Cu}_{0.6}$ electrode possessed a flat surface densely arranged by smooth spherical particles of size approximately 300 nm, appearing as a uniform film (Figures 1b and 3d–f). The size of the particles increased to approximately 500 nm for the $\text{Cu}_{1.2}$ electrode, and these particles were decorated by smaller particles with approximately 50 nm diameter (Figures 1c and 3j–l). Clear gaps between grainy particles with exposed substrates of bare FTO were observed (Figure 3a–c,g–i). The selective mapping in the 50 nm range showed that Cu and O elements were widely distributed on the plane for $\text{Cu}_{0.6}$, and the distribution of O was mostly localized compared to that of Cu (Figure 1b,d–f). In the precursor solution, Cu^{2+} ions were evenly dispersed in the absence of MEA. Under the effect of the electric field, Cu^{2+} ions were aligned in the solution and then moved to the cathode. The chemical reduction of considerable Cu^{2+} ions improved the anisotropic growth of microparticles. Cu^{2+} ions, as a transition metal, are inclined to bond to MEA to form $[\text{Cu}(\text{MEA})_2]^{2+}$ in the presence of MEA in the precursor solution [28]. The UV-vis absorption spectra of precursor solutions also demonstrated that the absorption edge of Cu^{2+} ions decreased and then the absorption peak of $[\text{Cu}(\text{MEA})_2]^{2+}$ rose as the addition of MEA increased, which illustrated that the Cu^{2+} ions were made more complex by MEA with $[\text{Cu}(\text{MEA})_2]^{2+}$ formation (Figure 4). Charged $[\text{Cu}(\text{MEA})_2]^{2+}$ moved directionally to the cathode; however, the higher mass of $[\text{Cu}(\text{MEA})_2]^{2+}$ slowed down its movement compared to Cu^{2+} , resulting in smaller particles by suppressing grain growth for $\text{Cu}_{0.6}$. However, the concentration of Cu^{2+} ions was reduced, and all of them were consumed after a large amount of MEA was added. Considerable amounts of $[\text{Cu}(\text{MEA})_2]^{2+}$ delayed the crystallization of Cu-based materials, and insufficient Cu^{2+} ions led to cracking on $\text{Cu}_{1.2}$. Atomic force microscopy (AFM) characterization further demonstrated that adding a suitable amount of MEA smoothed the surface of the $\text{Cu}_{0.6}$ electrode so that it became flat, with the lowest surface roughness compared to those of the Cu_0 and $\text{Cu}_{1.2}$ electrodes (Figure 5).

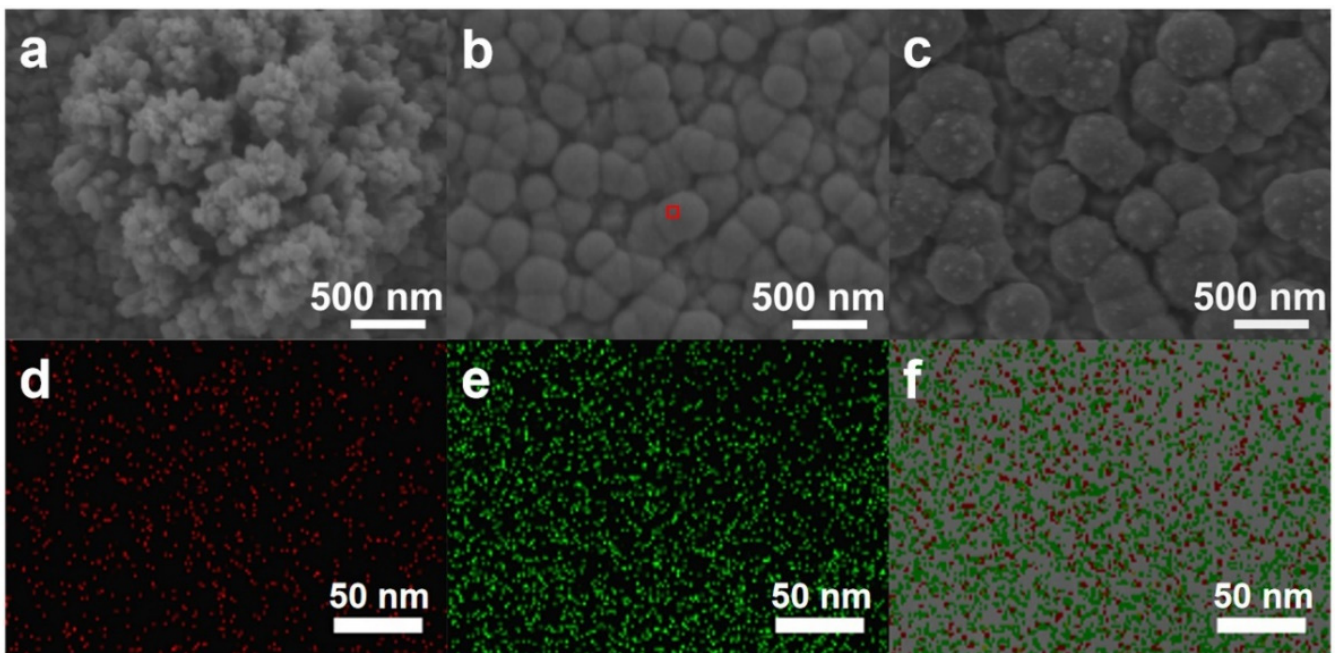


Figure 1. SEM images of the Cu-based electrodes: (a) Cu_0 , (b) $\text{Cu}_{0.6}$, and (c) $\text{Cu}_{1.2}$. Energy-dispersive spectrometry (EDS) mapping of $\text{Cu}_{0.6}$: (d) O, (e) Cu, and (f) O and Cu. The selected range of EDS is from the area circled with red frame in (b).

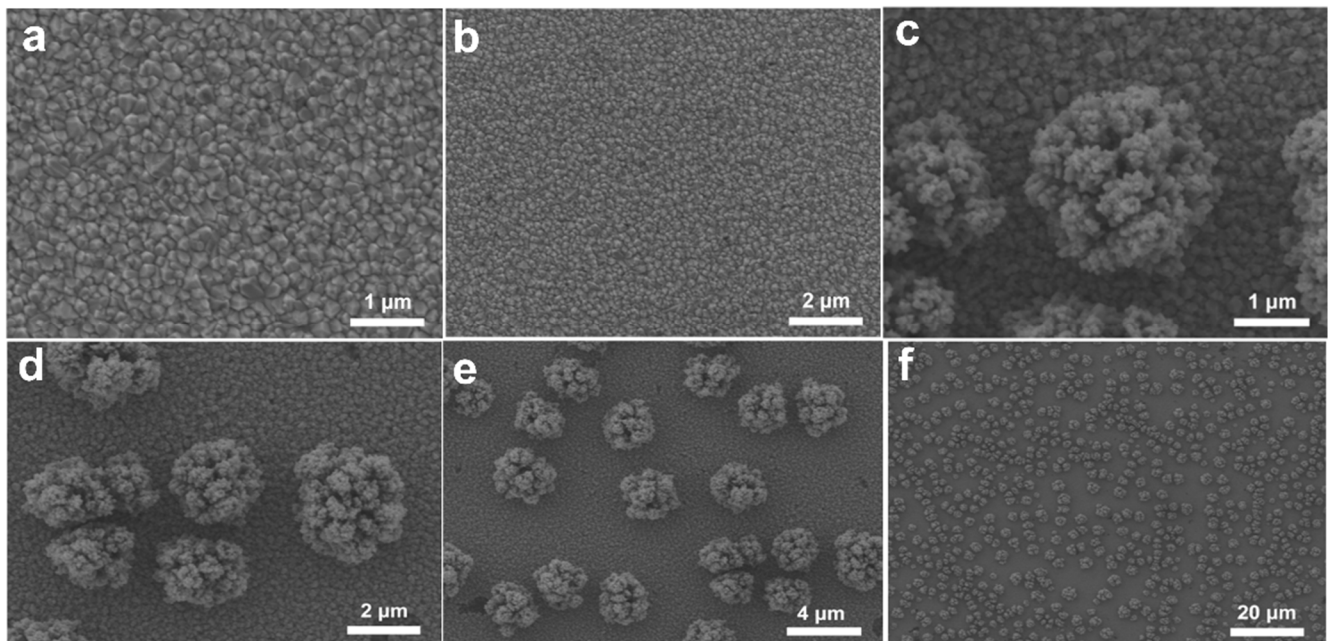


Figure 2. SEM images of the bared FTO with different scale bars: (a) $1\ \mu\text{m}$, (b) $2\ \mu\text{m}$. SEM images of Cu_0 with different scale bars: (c) $1\ \mu\text{m}$, (d) $2\ \mu\text{m}$, (e) $4\ \mu\text{m}$, (f) $20\ \mu\text{m}$.

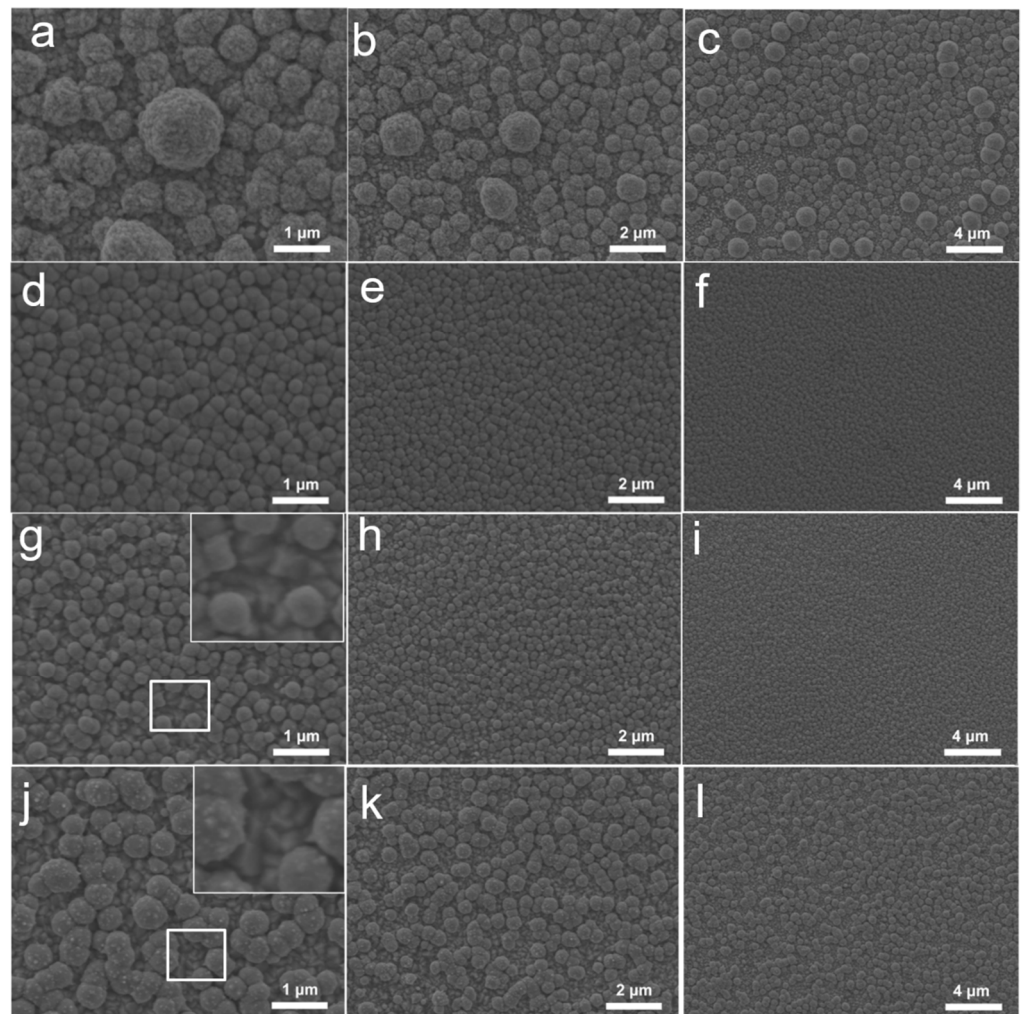


Figure 3. SEM images of the Cu-based electrodes with different scale bars for (a–c) $\text{Cu}_{0.3}$, (d–f) $\text{Cu}_{0.6}$, (g–i) $\text{Cu}_{0.9}$, and (j–l) $\text{Cu}_{1.2}$, inset images in (g,j) selected from the white squares, respectively.

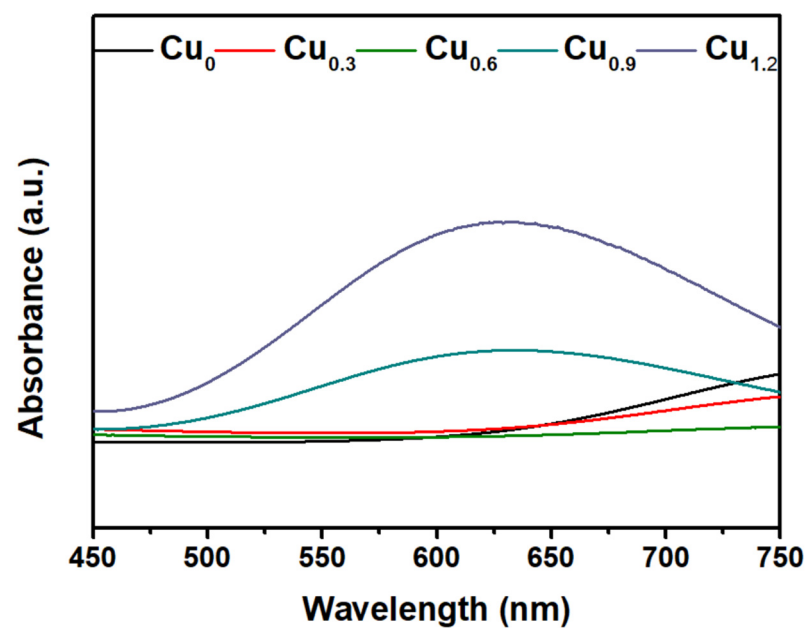


Figure 4. UV-vis absorption spectra of precursor solutions for Cu_0 , $\text{Cu}_{0.3}$, $\text{Cu}_{0.6}$, $\text{Cu}_{0.9}$, and $\text{Cu}_{1.2}$.

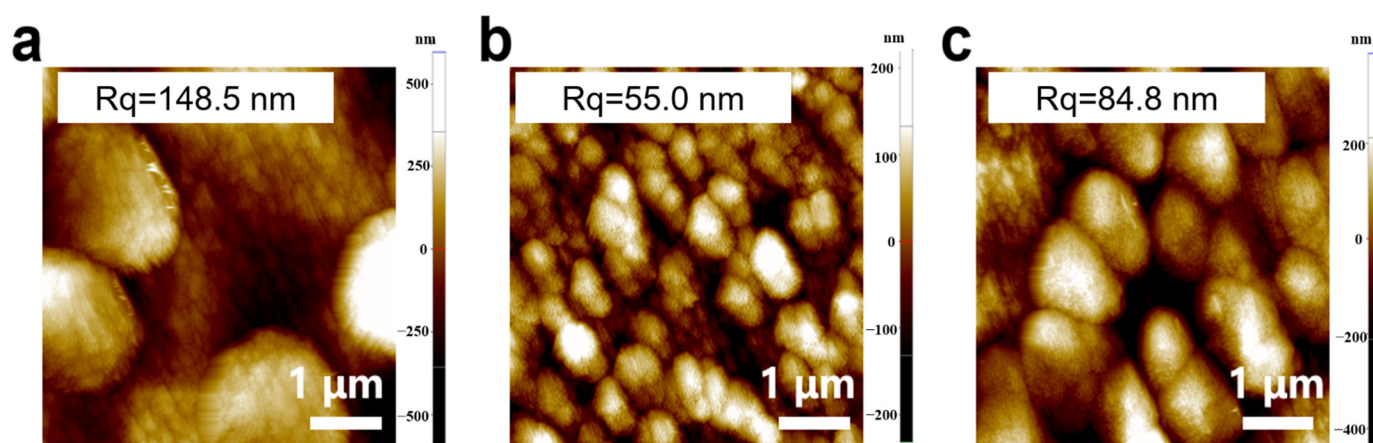


Figure 5. AFM images of copper-based electrodes: (a) Cu_0 , (b) $\text{Cu}_{0.6}$, (c) $\text{Cu}_{1.2}$.

2.2. The Phase Analysis of Cu-Based Electrodes

The X-ray diffraction (XRD) patterns of Cu-based electrodes clearly showed two peaks at 43.30° and 50.43° , corresponding to the (111) and (200) reflections of Cu (PDF#04-0836), respectively. The two peaks at 36.42° and 42.30° were attributed to the (111) and (200) reflections of Cu_2O (PDF#05-0667) (Figure 6a), respectively. The Cu_0 electrode exhibited stronger peaks of Cu, while the $\text{Cu}_{0.6}$ and $\text{Cu}_{1.2}$ electrodes exhibited the stronger peaks of Cu_2O . To confirm the coexistence of Cu^+ and Cu on a Cu-based electrode, an anodization experiment was conducted for the $\text{Cu}_{0.6}$ electrode. Two typical oxidation peaks at 0.16 V and 0.07 V vs. RHE were detected (Figure 6b), which were attributed to the oxidation of Cu^0 to Cu^{2+} and Cu^+ to Cu^{2+} , respectively [29].

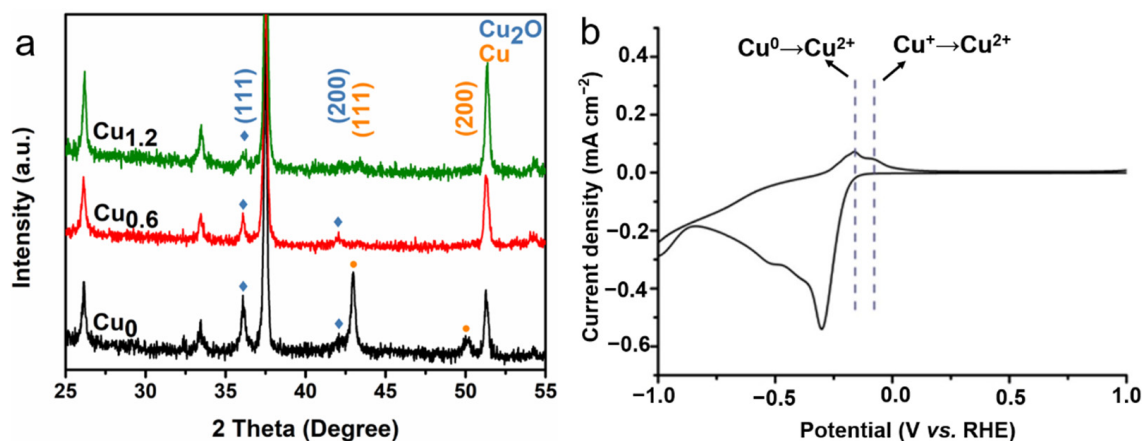


Figure 6. XRD patterns of the copper-based electrodes; unmarked peaks for FTO (a). CV for $\text{Cu}_{0.6}$ as the anode (b).

2.3. Electrochemical CO_2 Reduction for Cu-Based Electrodes

The performance of the CO_2RR was evaluated in a 0.1 M KHCO_3 saturated solution with potential ranging from -0.5 to -1 V (vs. RHE). Linear sweep voltammetry (LSV) was performed for the $\text{Cu}_{0.6}$ electrode, and it was found that the $\text{Cu}_{0.6}$ electrode exhibited a good activity for the electrochemical reduction of CO_2 with a higher current in the CO_2 -saturated electrolyte than in N_2 -saturated electrolyte (Figure 7). Compared to Cu_0 , H_2 generation was significantly inhibited on the $\text{Cu}_{0.6}$ and $\text{Cu}_{1.2}$ electrodes under all voltages. Moreover, ethanol generation was effectively improved at lower negative voltages, particularly for $\text{Cu}_{0.6}$, which exhibited the most favorable selectivity of ethanol (Figure 8a–c). At the potential of -0.6 V vs. RHE, the FE of $\text{Cu}_{0.6}$ for ethanol production was as high as 48%, which was optimal compared to those of most Cu-based electrodes

(Table 1). For the $\text{Cu}_{0.6}$ electrocatalyst, the yield of C_1 products (CO and formic acid) under all voltages did not exceed 15%, and the FE of H_2 was as low as 19%. Furthermore, the largest FE of C_2 products was 77% for the $\text{Cu}_{0.6}$ electrode at a potential of -0.6 V vs. RHE (Figures 8b and 9a–c), which was attributed to its stronger C–C coupling capability consuming the intermediate $^*\text{CO}$. However, the FE of the ethanol and C_2 products of the $\text{Cu}_{1.2}$ electrocatalyst was lower than those of $\text{Cu}_{0.6}$ under all voltages, which might be due to the surface structure of the $\text{Cu}_{1.2}$ electrocatalyst. In addition, the electrocatalytic performance of the $\text{Cu}_{0.3}$ and $\text{Cu}_{0.9}$ electrodes also verified that $\text{Cu}_{0.6}$ is the best electrocatalyst for ethanol production, as shown in Figure 9d,e. The stability of Cu-based electrodes in CO_2RR is of great significance for practical applications, considering the alkaline electrolyte and interface reliability. Continuous and stable operation of CO_2RR electrolysis was implemented on the $\text{Cu}_{0.6}$ electrode for 6 h under the voltage of -0.6 V vs. RHE. Moreover, no obvious changes in pH during the catalytic process (Figure 10a) was observed. The current remained above -0.5 mA cm^{-2} with a negligible decrease (Figure 10b–d), and the FE of ethanol was over 40% (Figure 8d) after 6h. The results of the SEM analysis of the $\text{Cu}_{0.6}$ electrode after the CO_2RR showed that the Cu-based material was well-maintained during the reaction (Figure 11a). Moreover, after the CO_2RR , still two oxidation peaks existed for $\text{Cu}_{0.6}$ as an anode, which suggested that the $\text{Cu}_{0.6}$ electrode was stable during the electrocatalytic process (Figure 11b). Although the current density was slightly lower, it could be significantly improved by atomic rearranging and a composite strategy.

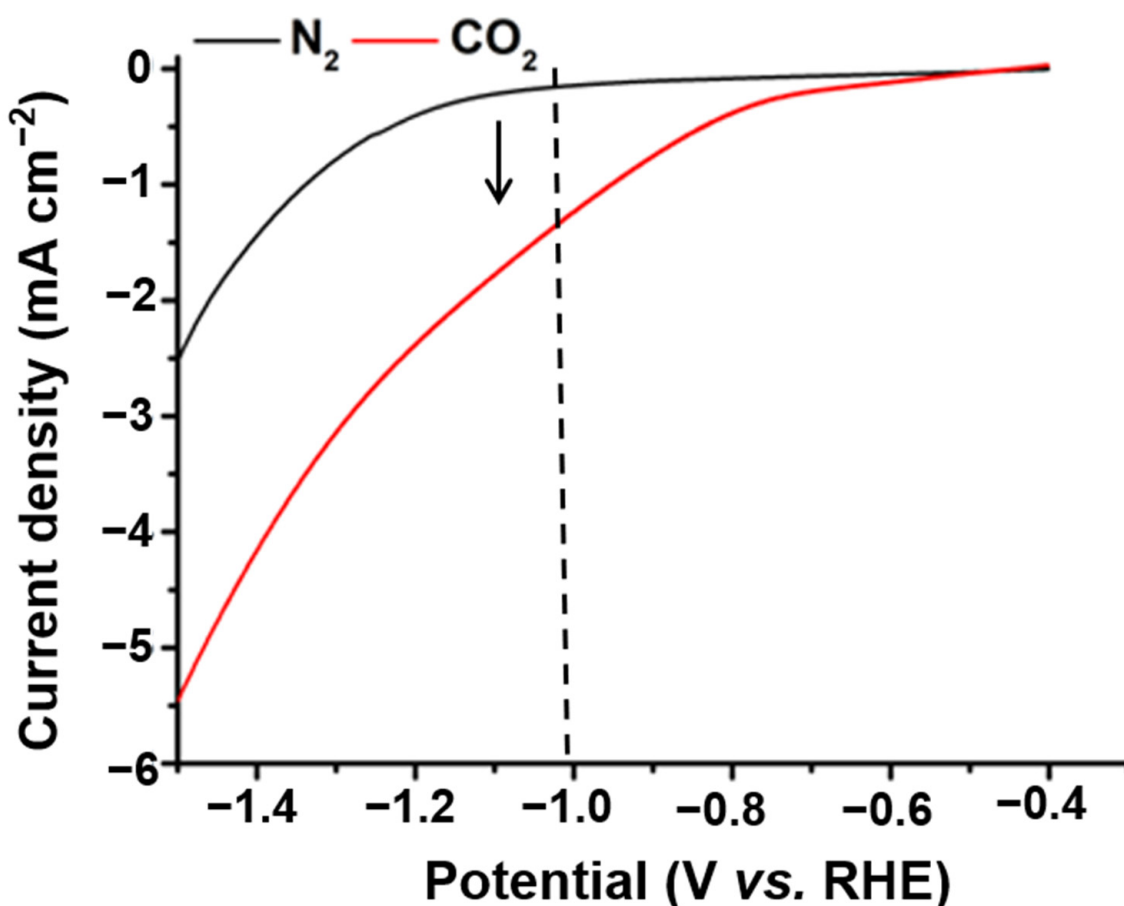


Figure 7. LSV curves of $\text{Cu}_{0.6}$ in the 0.1 M KHCO_3 solution saturated with N_2 (black) and CO_2 (red).

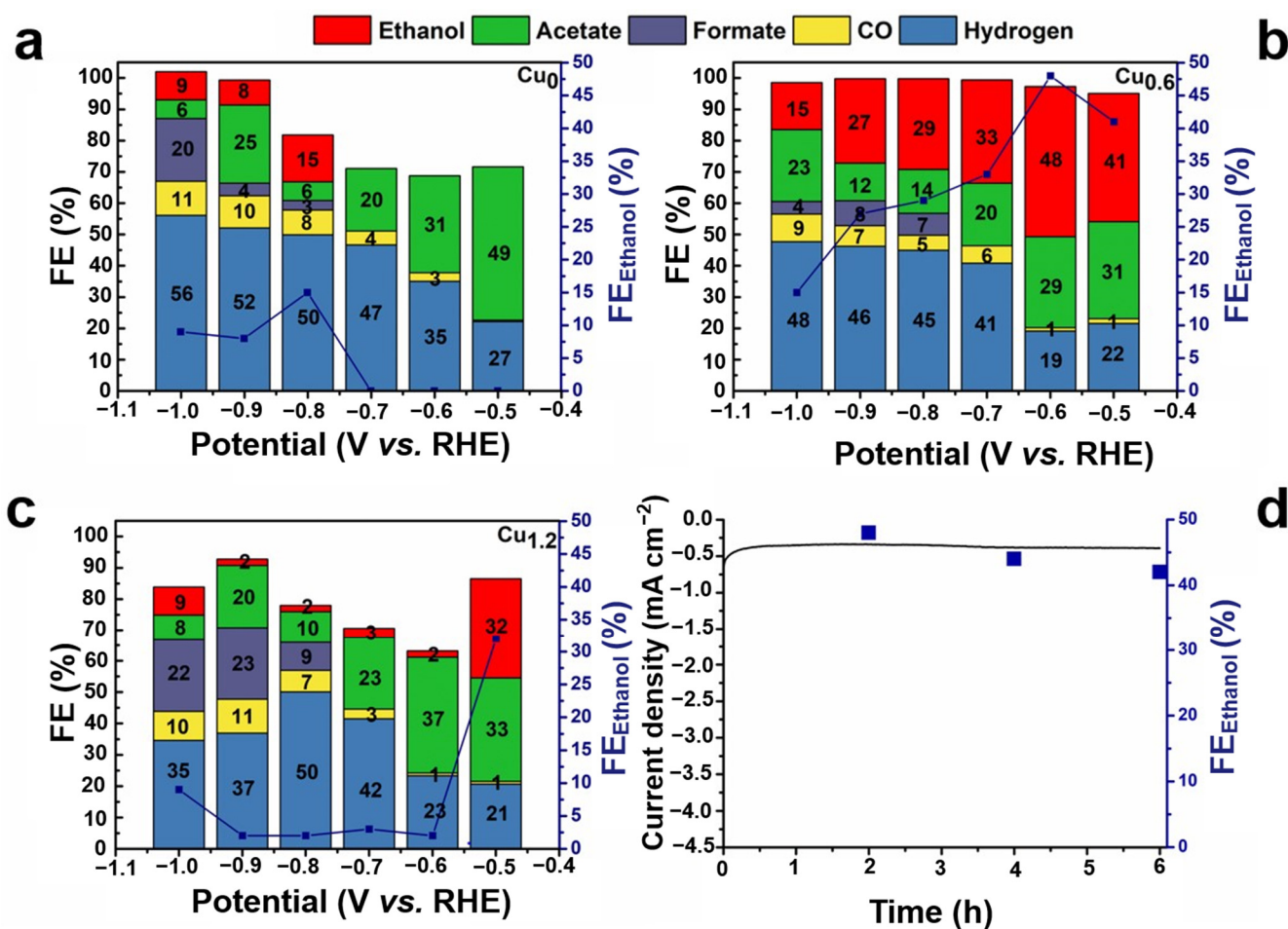


Figure 8. FEs of CO₂RR products for the (a) Cu₀, (b) Cu_{0.6}, and (c) Cu_{1.2} electrodes under different potentials. (d) Current stability and FE of ethanol under −0.6 V vs. RHE potential for 6 h.

Table 1. Comparison of ethanol and C₂ FE from recent reports and in our work.

| Catalyst | Electrolyte | FE (Ethanol)/% | FE (C ₂)/% | Ref. |
|---------------------------------------|-------------------------|----------------|------------------------|----------|
| Cu/Cu ₂ O | 0.1 M KCl | 41.2% | 81% | [12] |
| CuBr-DDT | 0.5 M KCl | 35.9% | 72% | [13] |
| Cu/Cu ₂ O-Ag-0.6 | 0.1 M KHCO ₃ | 19.2% | 60.9% | [16] |
| SD-CuCd ₂ | 0.1 M KHCO ₃ | 32% | - | [17] |
| Cu _{oh} -Ag | 0.1 M KHCO ₃ | 23.1% | 36.9% | [18] |
| Cu@Cu ₂ O | 0.1 M KHCO ₃ | 29% | 50% | [25] |
| np-Cu@VO ₂ -5% | 0.1 M KHCO ₃ | 30.1% | - | [26] |
| Au _{0.17} /Cu ₂ O | 0.1 M KHCO ₃ | 16.2% | - | [27] |
| Cu _{0.6} | 0.1 M KHCO ₃ | 48% | 77% | our work |

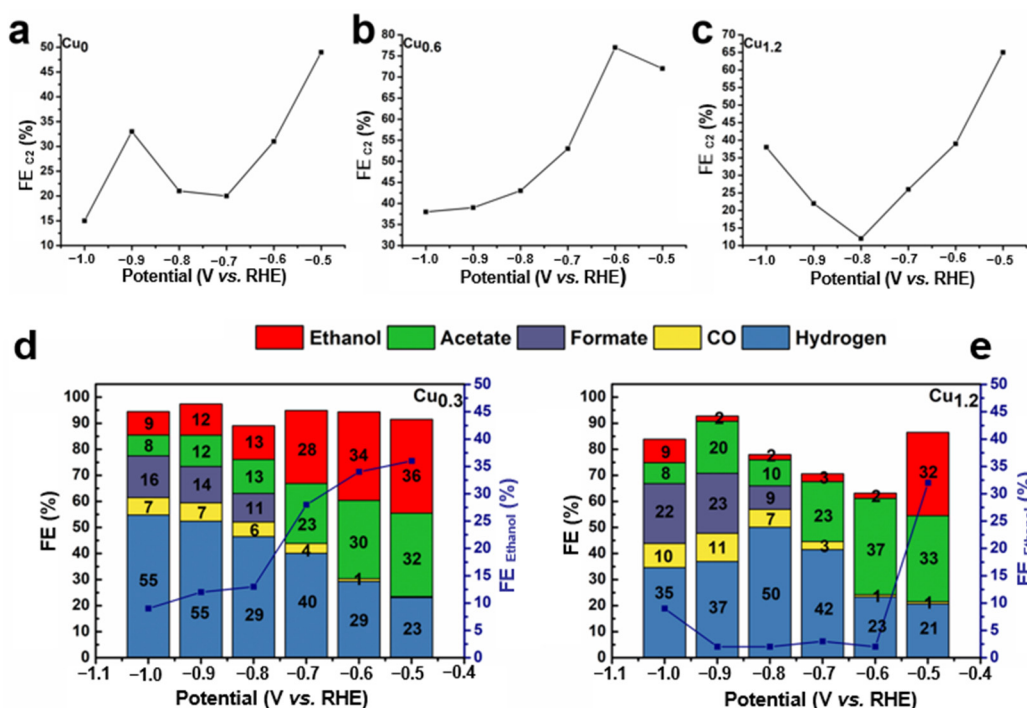


Figure 9. FE of C₂ for (a) Cu₀, (b) Cu_{0.6}, and (c) Cu_{1.2} under different potentials. FE of each CO₂ reduction products for (d) Cu_{0.3}, (e) Cu_{0.9} under different potentials.

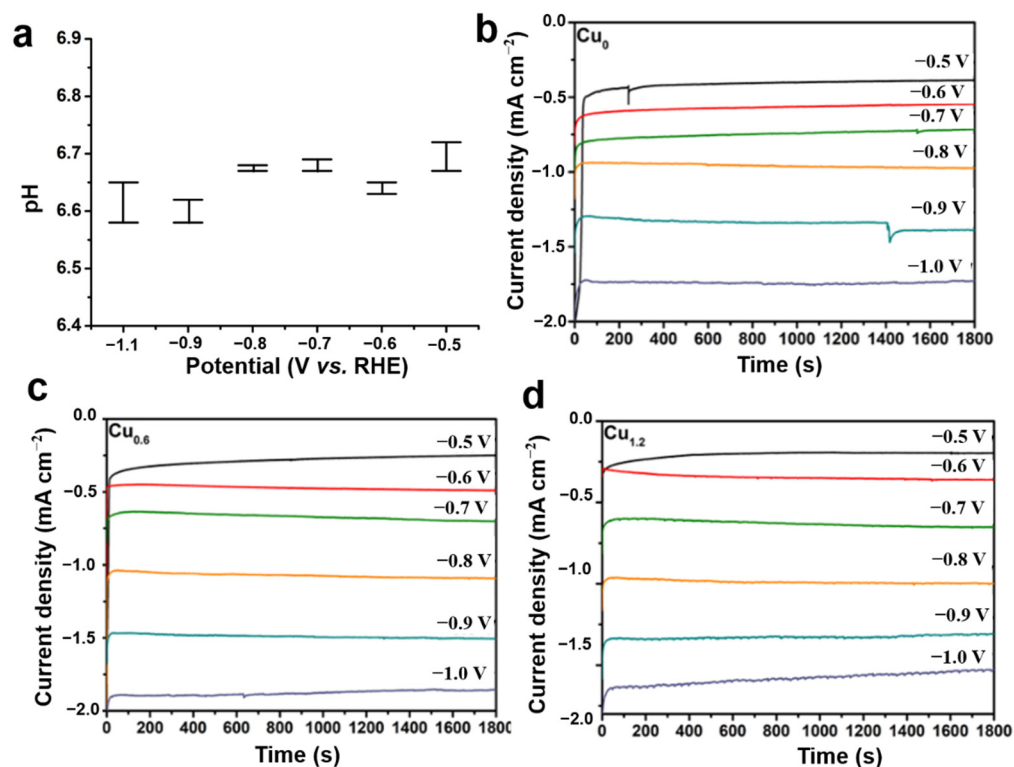


Figure 10. pH changes for Cu_{0.6} before and after the CO₂RR (a), the standard deviation no more than 0.02. Current densities for (b) Cu₀, (c) Cu_{0.6} and (d) Cu_{1.2} during CO₂RR.

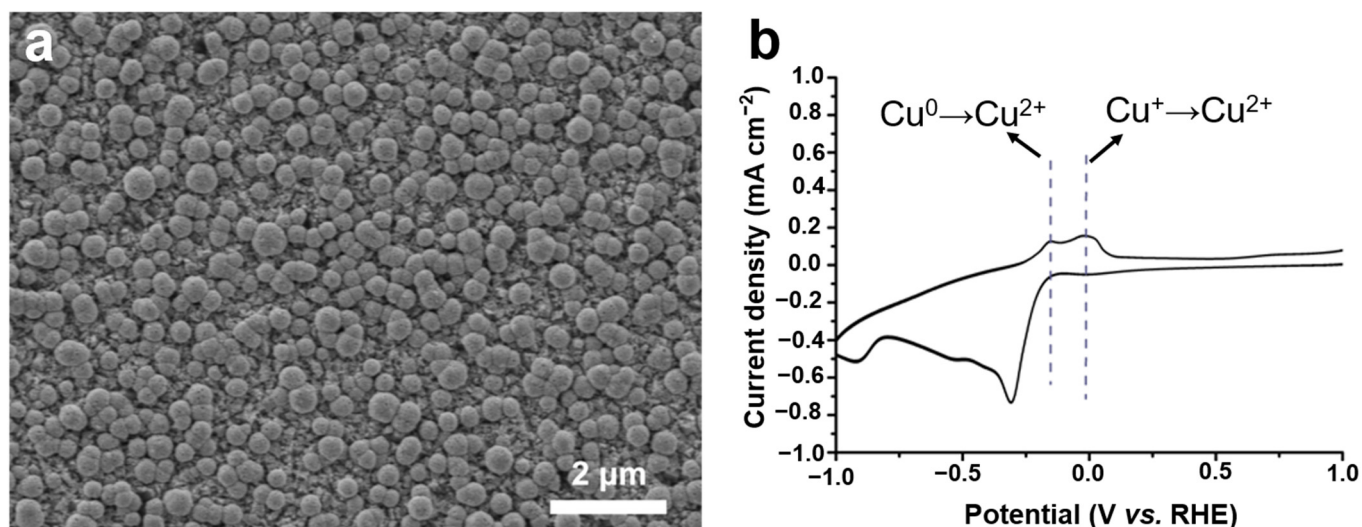


Figure 11. SEM images of $\text{Cu}_{0.6}$ after the CO_2RR (6 h) (a). CV for $\text{Cu}_{0.6}$ as anode after CO_2RR at -0.6 V vs. RHE (b).

2.4. Electrochemical Characterization of Cu-Based Electrodes

The ultraviolet-visible-near-infrared (UV-vis) spectrometry showed strong absorption of MEA and $[\text{Cu}(\text{MEA})_2]^{2+}$ at 200–320 nm, while no absorption for the $\text{Cu}_{0.6}$ electrode (Figure 12a) was observed in the same wavelength range. This indicated the presence of a Cu-based material and the absence MEA or $[\text{Cu}(\text{MEA})_2]^{2+}$ on the electrode. To study the dynamics of carriers, transient photoluminescence spectroscopy (TRPL) on Cu-based electrocatalysts was performed. Figure 12b shows that the fluorescence lifetime of $\text{Cu}_{0.6}$ was 0.117 ns, which was lower than those of Cu_0 (0.182 ns) and $\text{Cu}_{1.2}$ (0.130 ns). The shorter lifetime of the carriers in the $\text{Cu}_{0.6}$ electrode implied that the electrons quickly diffused to the interface, decreasing the non-radiative recombination of free electrons on the Cu-based electrodes. At the same time, the electrical impedance test also showed that the impedance of $\text{Cu}_{0.6}$ was the smallest (Figure 12c), indicating that the charge transfer resistance was the lowest in the $\text{Cu}_{0.6}$ electrode. The measurement of electrochemically active specific surface area (ECSA) indicated that the $\text{Cu}_{0.6}$ electrocatalyst was capable of providing higher catalytic activity (Figure 13a–d). At the same time, the kinetic resistance of the catalyst for CO_2RR was smaller for the $\text{Cu}_{0.6}$ electrode with a smaller Tafel slope (Figure 12d). To explore the main cause of ethanol production for the Cu-based electrodes, we calcined the $\text{Cu}_{0.6}$ electrode in Ar and air atmosphere (Figure 13e). For the $\text{Cu}_{0.6}$ electrode post-treated in the Ar atmosphere, the obvious generation of ethanol (FE, 32%) and hydrogen (Figure 12d) was observed. However, no ethanol was detected for the $\text{Cu}_{0.6}$ electrode temperature-treated in air, which was in an oxidized state without oxidation peaks (Figure 13f). The surface redox state of Cu was closely related to the CO_2RR performance of the Cu-based electrodes.

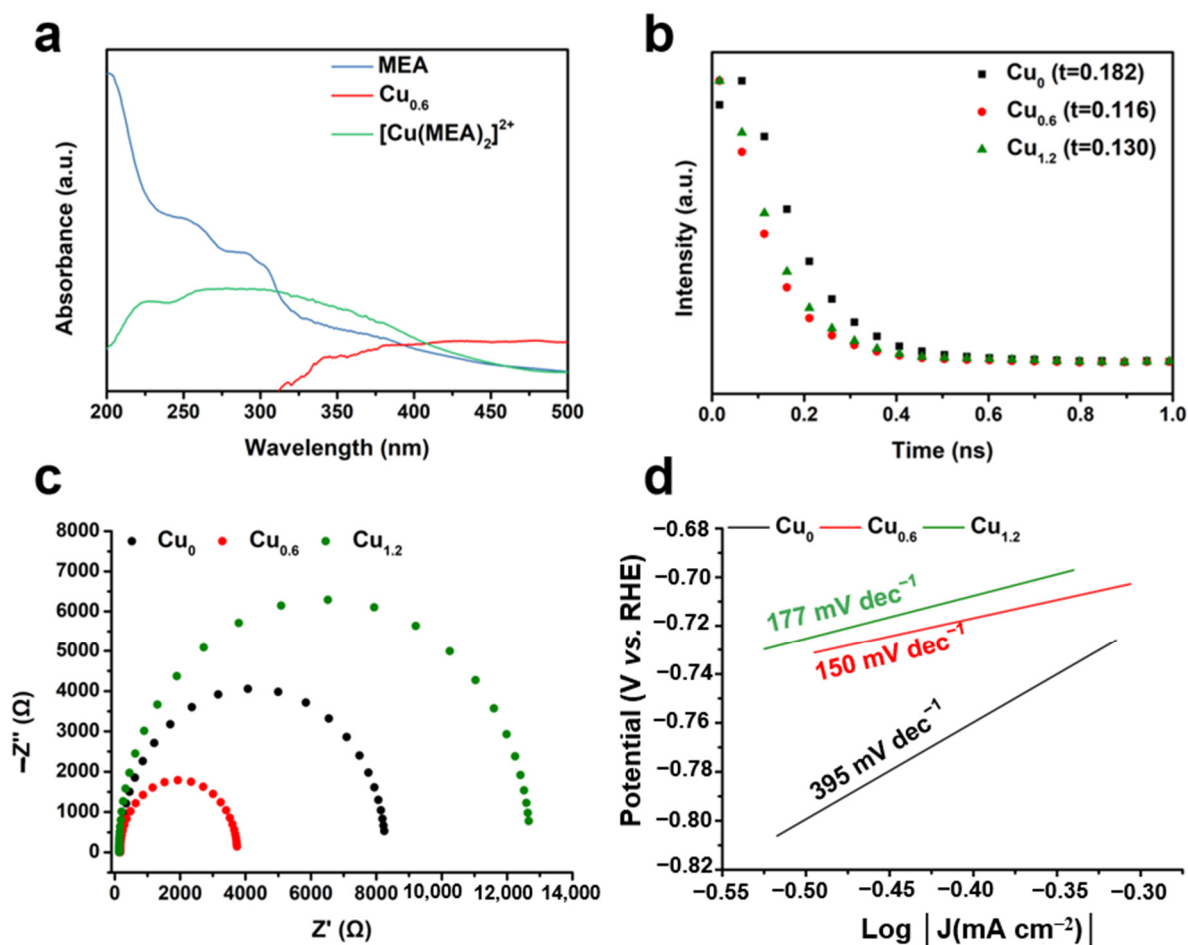


Figure 12. (a) UV-vis spectra of MEA (blue), Cu_{0.6} (red), and [Cu(MEA)₂]²⁺ (green). (b) Fluorescence decay spectra of Cu₀ (black), Cu_{0.6} (red), and Cu_{1.2} (green). (c) Electrochemical impedance spectroscopy (EIS) of Cu₀ (black), Cu_{0.6} (red), and Cu_{1.2} (green). (d) Tafel slopes of Cu₀ (black), Cu_{0.6} (red), and Cu_{1.2} (green).

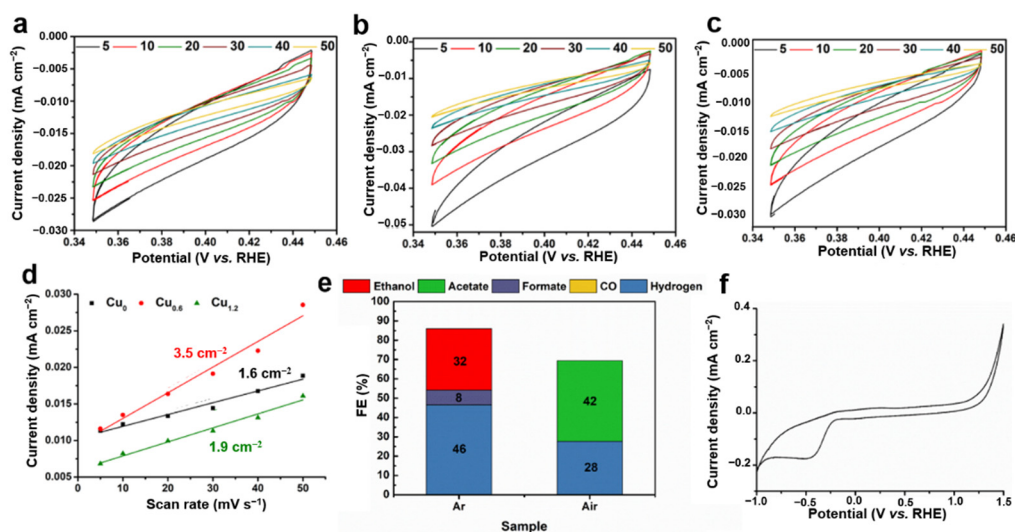


Figure 13. ECSA for (a) Cu₀, (b) Cu_{0.6}, (c) Cu_{1.2}, and the electrochemical surface area for (d) Cu₀ (black), Cu_{0.6} (red), and Cu_{1.2} (green). FE of the CO₂RR products for Cu_{0.6} post-treated under different atmospheres at -0.6 V vs. RHE (e). CV of Cu_{0.6} post-treated in air at 150 °C for 6 h as the anode (f).

2.5. X-ray Photoelectron Spectroscopy of Cu-Based Materials

Fine X-ray photoelectron spectroscopy (XPS) of Cu 2p in a Cu-based electrode was performed to analyze the valence state of Cu on the surface (Figure 14a,b). It is difficult to distinguish between Cu^+ and Cu^0 from the Cu 2p_{1/2} and Cu 2p_{3/2} peaks [30]. For Cu 2p_{3/2} and O 1s spectra, there was only one peak for each spectral line, which also demonstrated that the individual oxide of Cu_2O exists in Cu-based material instead of CuO [31]. Further analysis with Cu LMM Auger energy spectrum (AES) demonstrated that Cu^+ and Cu^0 coexist on the electrodes (Figure 14c), and Cu^+ ions are dominated at the peak of approximately 569.8 eV compared to 568.0 eV for Cu^0 ions and 565.2 eV for the transition state of the Cu LMM [32]. These corresponding peaks were integrated to determine the ratio between Cu^+ and Cu^0 ions. For these as-prepared electrodes, the concentration ratio of Cu^+ and Cu^0 ions increased from 1.24/1 to 1.54/1 with increasing MEA content (Figure 14d–f). The strong interaction between Cu^{2+} and MEA affected the reduction of Cu^{2+} to Cu^+ and further to Cu^0 by Cu^+ [33]. For the $\text{Cu}_{0.6}$ electrode, the medium concentration ratio was 1.42/1, which showed the predominant CO_2RR performance. The above AES characterizations were implemented on the flaking Cu-based powders. In addition, the AES of the electrodes was achieved, and it showed only the peak of Cu^+ without Cu^0 (Figure 15), which could be probably attributed to the localized distribution of Cu_2O and Cu. Moreover, the electrode surface (0–5 nm depth) was covered by Cu_2O . The product selectivity could be probably attributed to the synergy between Cu^+ and Cu^0 ions, which was demonstrated to accelerate CO_2 activation and CO dimerization [26]

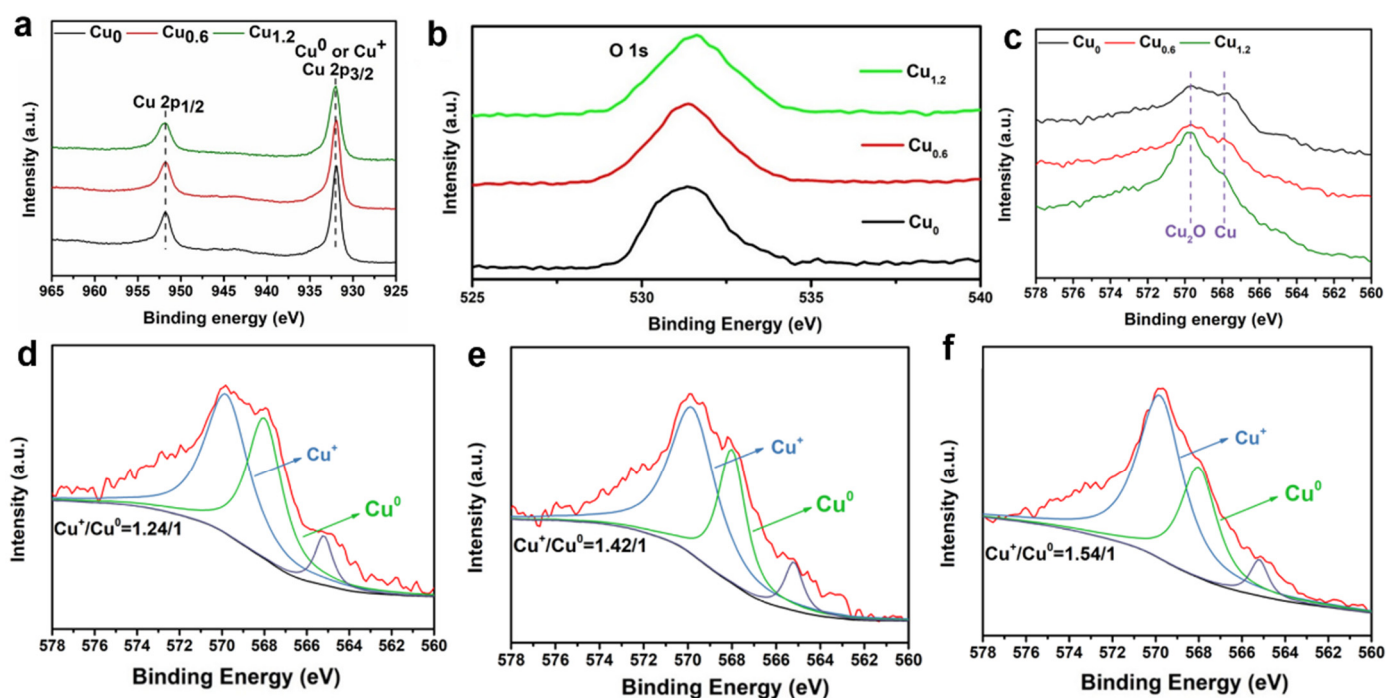


Figure 14. XPS peaks (a) Cu 2p and (b) O 1s of Cu_0 (black), $\text{Cu}_{0.6}$ (red), $\text{Cu}_{1.2}$ (green). (c) Cu LMM Auger energy spectra of Cu_0 (black), $\text{Cu}_{0.6}$ (red), and $\text{Cu}_{1.2}$ (green) flaking powders. Cu 2p_{3/2} split peaks for (d) Cu_0 , (e) $\text{Cu}_{0.6}$, and (f) $\text{Cu}_{1.2}$.

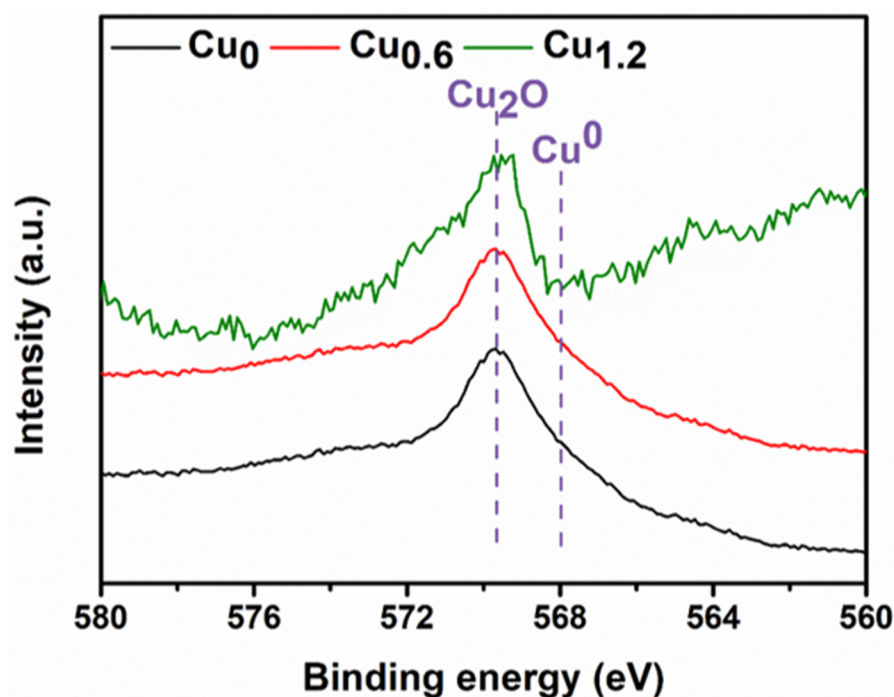


Figure 15. Cu LMM Auger energy spectra of Cu₀ (black), Cu_{0.6} (red), Cu_{1.2} (green) electrodes.

2.6. The Formation of *CO Intermediate for Ethanol Production

The details of the valence state of Cu and its relationship with the *CO intermediate in CO₂RR are worth exploring to obtain electrocatalysts with enhanced activity and high selectivity. The stable existence of the initial *CO intermediate played a significant role in C–C coupling, and it could be calculated using density functional theory simulations. The atomic structure models were implemented and *CO intermediates were bonded to the Cu atoms (Figure 16a–c). The degree of stability was represented by the free energy of the *CO intermediate. The free energy of *CO intermediate was -3.03 eV for Cu_{0.6}, which was significantly lower than those for Cu₀ (-1.85 eV) and Cu_{1.2} (-2.20 eV), indicating that the *CO intermediate was more stable on Cu_{0.6} than on Cu₀ and Cu_{1.2}. The stable existence of *CO significantly contributes to C–C coupling by the supply of the reaction precursor [34]. To date, there is no definite reactive process for CO₂RR to ethanol. We propose one probable route considering the reported work (Figure 16d) [19,25,34,35]. The Cu_{0.6} electrode probably achieves the balance between *CO–Cu⁺ (containing positively charged C) and *CO–Cu⁰ (containing negatively charged C) [25]. The electrostatic attraction between these two C atoms contributes to the formation of the C–C bond. In addition to abundant *CO intermediates, adequately monoprotonated *CHO intermediates exist on the electrode, and they are prone to forming *CO–COH intermediates [34]. The CO–COH intermediates then accept multi-protons and electrons to obtain the precursor (*CH₂CH₂OH) of the final product ethanol [19,35]. The high specific surface area of Cu_{0.6} provides abundant reaction sites for the CO₂RR and an appropriate Cu⁺/Cu⁰ ratio that accumulates reaction intermediates. The high concentration of the *CO intermediates on the Cu⁰–Cu⁺ interface further promotes the C–C dimerization reaction and improves the selectivity of ethanol.

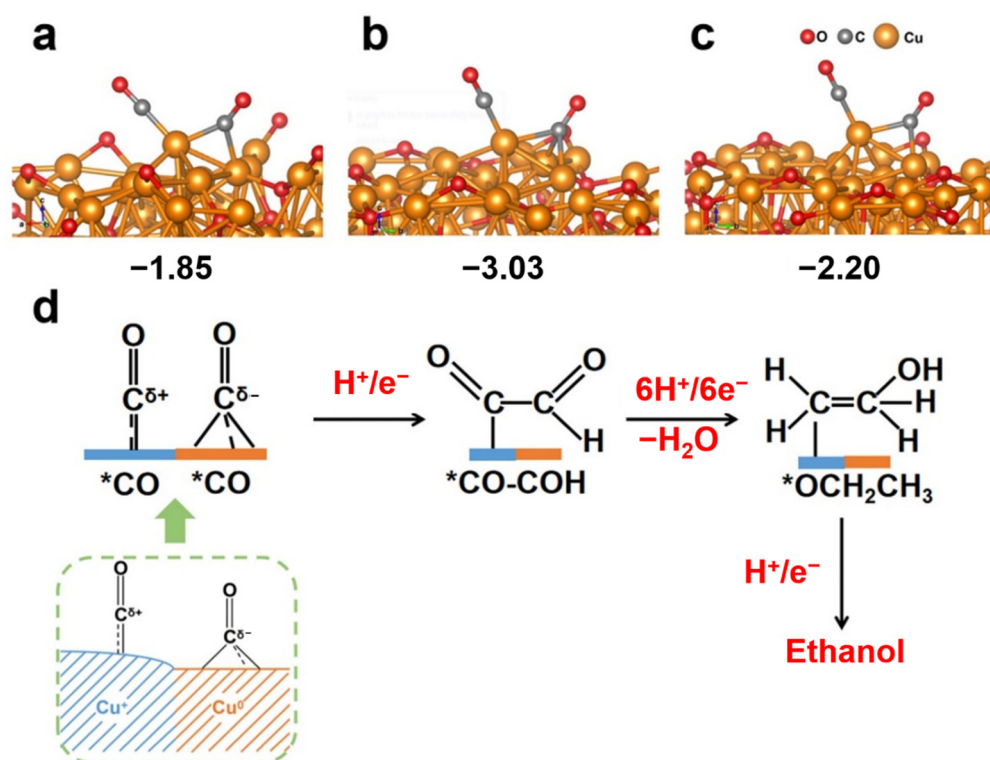


Figure 16. Free energy of *CO formation for (a) Cu₀, (b) Cu_{0.6}, and (c) Cu_{1.2}. (d) Scheme of the reaction pathway of a CO₂RR.

3. Materials and Methods

Synthesis of Cu-based electrodes on FTO: The Cu-based electrodes were prepared using a one-step electrochemical deposition method on FTO. The three-electrode cell—Ag/AgCl as the reference electrode, FTO as the working electrode, and counter electrode—was used. Before the deposition, the bare FTO substrates were ultrasonically cleaned with isopropanol, ethanol, and water 6 times and quickly dried with nitrogen gas. Simultaneously, a definite volume of MEA (0, 60, 120, 180, and 240 μ L) was dropped into a copper nitrate solution (0.1 mmol, 20 mL) as the deposited electrolyte. Then, the three-electrode cell was operated in the prepared electrolyte at a constant voltage of -0.4 V vs. RHE for 30 s, and five Cu-based electrodes were obtained in five precursor solutions with different volumes of MEA. The as-prepared electrodes were flushed with water three times and finally dried with nitrogen gas.

Characterization: The images were obtained using SEM (jsm-7800F, JEOL, Japan), and the SEM mapping was acquired using an energy-dispersive spectrometer in the same instrument. AFM analysis was conducted using an atomic force microscope (XE-70, Park systems, Korea). The XRD patterns of the samples were collected with a Smartlab (3 KW) X-ray powder diffractometer, and the Cu-K- α radiation wavelength was 0.154178 nm. Moreover, UV-vis spectra were collected using an ultraviolet spectrophotometer (PE Lambda 950, PerkinElmer, U.S.). TRPL analysis was conducted using a time-resolved fluorescence spectrometer (FLS 980, Edinburgh, UK). The XPS data were obtained using a K-alpha X-ray photoelectron spectrometer (PHI5000 Versaprobe, ULVAC-PHI, Japan). The pH of the solution was measured using Sartorius PB-10 (Sartorius, German).

Electrochemical measurements: An electrochemical workstation (CHI660E, Shanghai Chenhua, China) was used for electrochemical measurements. In the CO₂RR characterization, the platinum electrode was used as the counter electrode, Ag/AgCl (saturated KCl) as the reference electrode, and the Cu-based electrode as the working electrode to form a three-electrode system. A proton exchange membrane (Nafion 117, Sigma-Aldrich, German) was inserted in the middle of electrolyte to ensure that only hydrogen ions could

pass through the membrane (Figure 17). Further, 100 mL of 0.1 mmol KHCO_3 solution was added to the reactor as the electrolyte with the remaining 150 mL of headspace volume. Before the reaction, high-purity carbon dioxide (99.99%) gas was vented into the electrolyte for 30 min to reach saturation.

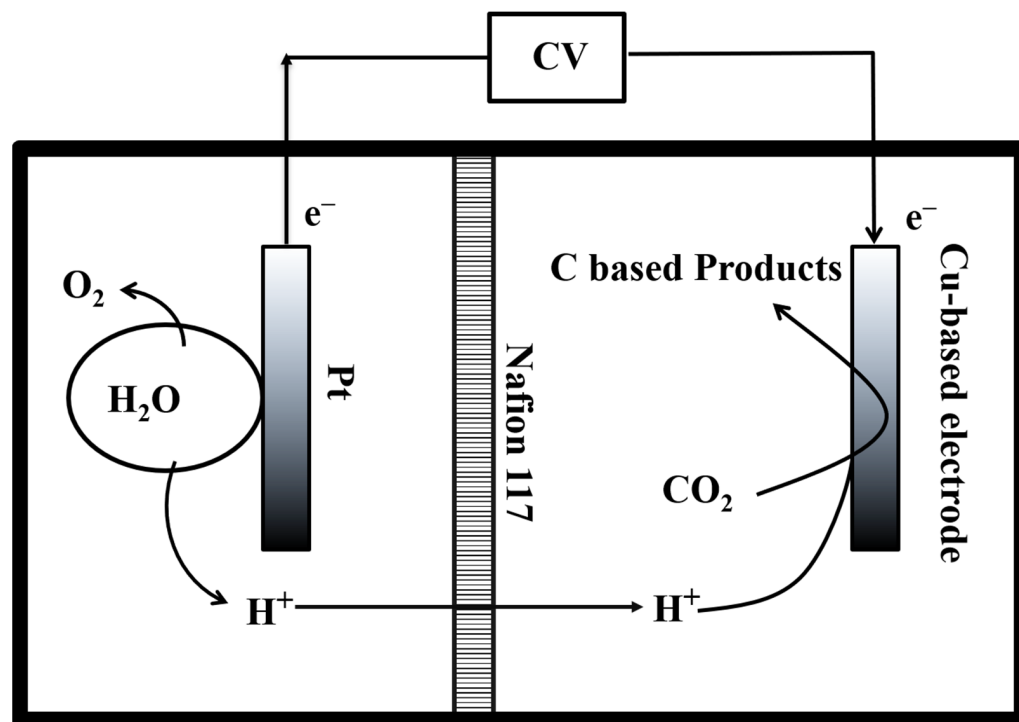


Figure 17. The scheme of CO_2RR system for Cu-based electrodes.

All the potentials were converted to relative potentials according to the RHE reference value: $E(\text{vs RHE}) = E\left(\text{vs } \frac{\text{Ag}}{\text{AgCl}}\right) + 0.197 \text{ V} + 0.0592\text{pH V}$.

Identification and quantification of gaseous products: Gas chromatography (GC-9860-5C-NJ, Hao Erpu, China) was used to analyze the gas products, with argon (99.99%) as the carrier gas. A series of definite concentrations of gas were injected into the gas chromatograph (GC) to obtain the calibrated concentration of the gas products (H_2 , CO , CH_4 , C_2H_4 , C_2H_6). Carbon-based gases and H_2 were detected using a flame ionization detector and a thermal conductivity detector, respectively. Moreover, 1 mL of reactive gas was extracted each time and quickly injected into the GC for analysis.

Identification and quantification of liquid products: All the liquid products were quantified using a nuclear magnetic resonance spectrometer (JNM-ECZ400S/L1, JEOL, Japan). Different concentrations (0.5, 1, 1.5, 2, 2.5, 3, 3.5, and 4 mmol/L) of formic acid, methanol, acetic acid, and ethanol were prepared to obtain a correlation between the concentration and the peak intensity of the ^1H spectra. Specifically, 400 μL of the above solution was mixed with 200 μL of deuterated dimethyl sulfoxide (d-DMSO, Adamas, German) nuclear magnetic sample, and presaturation was used for water suppression during the NMR spectrum test. The standard curve was obtained considering the product concentration and NMR spectrum. The product concentration was presented along the abscissa and the NMR peak intensity along the ordinate, with the deuterated peak as consultation (Figure 18).

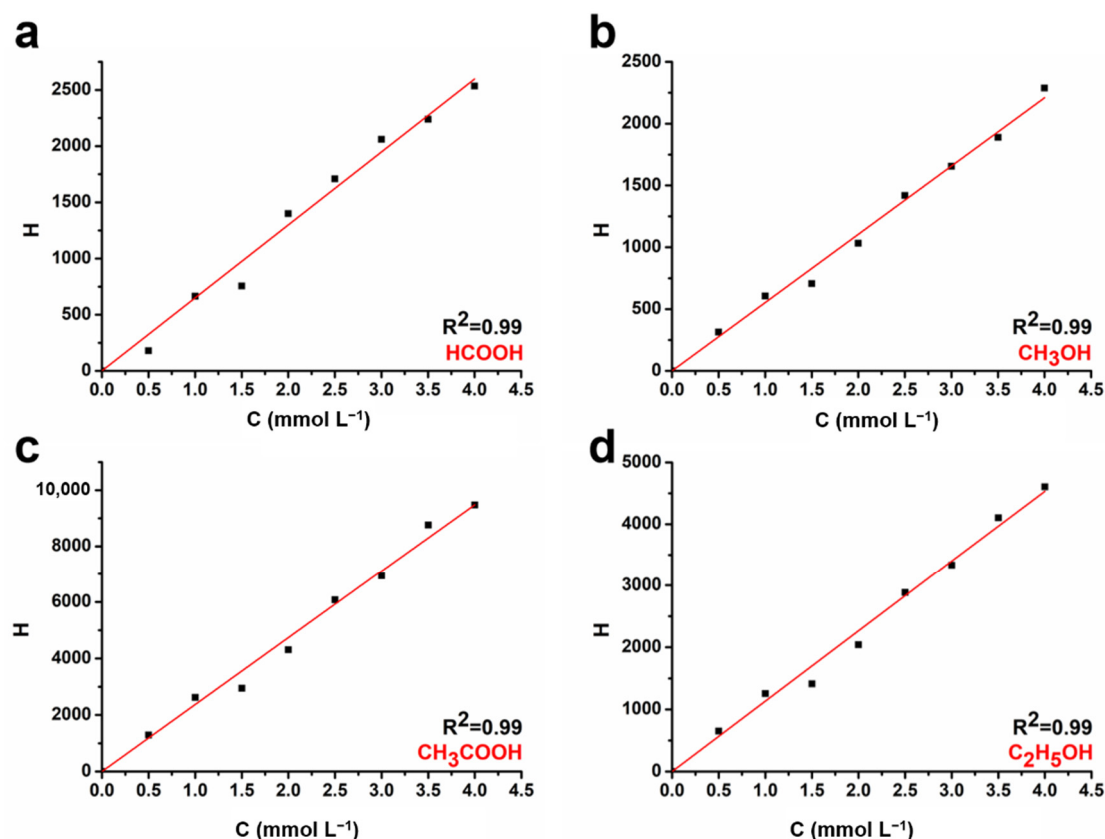


Figure 18. Standard curve lines of (a) HCOOH, (b) CH₃OH, (c) CH₃COOH, (d) C₂H₅OH.

The FE for the formation of all the products (both gas and liquid products) was calculated as follows: $FE = n \times e \times N_A \times \frac{q}{Q} = n \times e \times N_A \times q / (I \times t)$, where n is the total amount of product (in moles), e is the number of electrons transferred, N_A is the Avogadro constant, q is the elementary charge, Q is the charge, I is the current, and t is the running time.

Computational method: We have employed the Vienna ab initio simulation package (VASP) [36,37] to perform all density functional theory (DFT) calculations within the generalized gradient approximation (GGA) using the Perdew-Burke-Ernzerhof (PBE) [38] formulation. We have chosen the projected augmented wave (PAW) potentials [39,40] to describe the ionic cores and take valence electrons into account using a plane wave basis set with a kinetic energy cutoff of 450 eV. Partial occupancies of the Kohn–Sham orbitals were allowed using the Gaussian smearing method and a width of 0.05 eV. The electronic energy was considered self-consistent when the energy change was smaller than 10^{-6} eV. A geometry optimization was considered convergent when the force change was smaller than 0.03 eV/Å. Grimme’s DFT-D3 methodology [41] was used to describe the dispersion interactions. The Brillouin zone was sampled with a gamma-centered grid $2 \times 2 \times 1$ through all the computational process. Periodic boundary conditions were used in all directions and a vacuum layer of 15 Å was used in the z-direction to separate the slabs.

The adsorption energy (E_{ads}) of adsorbate molecule was defined as $E_{ads} = E_{mol/surf} - E_{surf} - E_{mol}$, where $E_{mol/surf}$, E_{surf} and E_{mol} (g) are the energy of adsorbate molecule adsorbed on the surface, the energy of clean surface, and the energy of isolated molecule in a cubic periodic box, respectively.

4. Conclusions

Cu-based electrodes were fabricated by a one-step electrodeposition method using MEA as a morphology and valence state agent. Moreover, the electrodes were used for electrochemical CO₂RR. The addition of MEA smoothed the surface of the Cu-based

electrodes and simultaneously modulated the valence state of the Cu element. The Cu_{0.6} electrode had a flat surface and a superior concentration ratio of Cu⁺ and Cu⁰ ions, which significantly improved the electrochemical efficiency and ethanol production in the CO₂RR. For the Cu_{0.6} electrode, the maximum FE of ethanol was up to 48% at a potential of −0.6 V vs. RHE, which is also the largest value for single-material catalysts. At the same voltage, the overall C₂ selectivity was above 77%. The flat surface significantly shortened the transfer time of electrons from the electrode to the reactive surface. At the same time, the Cu_{0.6} electrode exhibited the optimal Cu⁺/Cu⁰ concentration ratio of 1.42/1 compared to Cu₀ and Cu_{1.2}, which can stabilize the *CO intermediates with the lowest free energy. The synergistic effect of Cu⁺ and Cu⁰ is advantageous for the C–C coupling formed by the dimerization of carbon intermediates. The possible mechanism is that the C atoms bonding to Cu⁺ and Cu⁰ have opposite electrical charges, and the C–C bond is favorably formed under the effect of the electric field, that is, due to the electrostatic attraction. This study provides an efficacious guide to fabricating efficient electrocatalysts, which has potential significance for product selectivity in the CO₂RR.

Author Contributions: Conceptualization, H.L. and P.L.; methodology, P.L.; software, H.L.; validation, H.L., Y.Z. and G.W.; formal analysis, H.L.; investigation, H.L.; resources, G.W.; data curation, Y.Z.; writing—original draft preparation, H.L.; writing—review and editing, A.S.W.; visualization, J.W. and Q.M.; supervision, P.L.; project administration, P.L.; funding acquisition, P.L. All authors have read and agreed to the published version of the manuscript.

Funding: This research was funded by the National Natural Science Foundation of China, 21802071, and the National Natural Science Foundation of Jiangsu Province, BK20170979.

Institutional Review Board Statement: Not applicable.

Informed Consent Statement: Not applicable.

Data Availability Statement: The data supporting reported results are available on request from the corresponding author.

Acknowledgments: The authors thank Yonghua Chen for paper revision and Gang Lu for spectral analysis.

Conflicts of Interest: The authors declare no conflict of interest.

References

1. Wang, P.; Yang, H.; Xu, Y.; Huang, X.; Wang, J.; Zhong, M.; Cheng, T.; Shao, Q. Synergized Cu/Pb Core/Shell Electrocatalyst for High-Efficiency CO₂ Reduction to C₂₊ Liquids. *ACS Nano* **2021**, *15*, 1039. [[CrossRef](#)] [[PubMed](#)]
2. Lamaison, S.; Wakerley, D.; Kracke, F.; Moore, T.; Zhou, L.; Lee, D.U.; Wang, L.; Hubert, M.A.; Aviles Acosta, J.E.; Gregoire, J.M.; et al. Designing a Zn-Ag Catalyst Matrix and Electrolyzer System for CO₂ Conversion to CO and Beyond. *Adv. Mater.* **2021**, *34*, 2103963. [[CrossRef](#)] [[PubMed](#)]
3. Xie, H.; Wan, Y.; Wang, X.; Liang, J.; Lu, G.; Wang, T.; Chai, G.; Adli, N.M.; Priest, C.; Huang, Y.; et al. Boosting Pd-Catalysis for Electrochemical CO₂ Reduction to CO on Bi-Pd Single Atom Alloy Nanodendrites. *Appl. Catal. B* **2021**, *289*, 119783. [[CrossRef](#)]
4. Xue, L.; Zhang, A.; Wu, J.; Wang, Q.; Liu, Y.; Zhao, Y.; Liu, S.; Liu, Z.; Li, P.; Zeng, S. Surface Modification and Reconstruction of ZnO Hollow Microspheres for Selective Electroreduction of CO₂ to CO. *J. Alloys Compd.* **2021**, *882*, 160703. [[CrossRef](#)]
5. Tian, J.; Wang, R.; Shen, M.; Ma, X.; Yao, H.; Hua, Z.; Zhang, L. Bi-Sn Oxides for Highly Selective CO₂ Electroreduction to Formate in a Wide Potential Window. *ChemSusChem* **2021**, *14*, 2247. [[CrossRef](#)]
6. Mohamed, A.G.A.; Zhou, E.; Zeng, Z.; Xie, J.; Gao, D.; Wang, Y. Asymmetric Oxo-Bridged ZnPb Bimetallic Electrocatalysis Boosting CO₂-to-HCOOH Reduction. *Adv. Sci.* **2021**, *9*, 2104138. [[CrossRef](#)]
7. Huang, M.; Gong, S.; Wang, C.; Yang, Y.; Jiang, P.; Wang, P.; Hu, L.; Chen, Q. Lewis-Basic EDTA as a Highly Active Molecular Electrocatalyst for CO₂ Reduction to CH₄. *Angew. Chem. Int. Ed.* **2021**, *60*, 23002. [[CrossRef](#)]
8. Lu, L.; Sun, X.; Ma, J.; Yang, D.; Wu, H.; Zhang, B.; Zhang, J.; Han, B. Highly Efficient Electroreduction of CO₂ to Methanol on Palladium-Copper Bimetallic Aerogels. *Angew. Chem. Int. Ed.* **2018**, *57*, 14149. [[CrossRef](#)]
9. Lu, Y.F.; Dong, L.Z.; Liu, J.; Yang, R.X.; Liu, J.J.; Zhang, Y.; Zhang, L.; Wang, Y.R.; Li, S.L.; Lan, Y.Q. Predesign of Catalytically Active Sites via Stable Coordination Cluster Model System for Electroreduction of CO₂ to Ethylene. *Angew. Chem. Int. Ed.* **2021**, *60*, 26210. [[CrossRef](#)]
10. Aran-Ais, R.M.; Scholten, F.; Kunze, S.; Rizo, R.; Cuenya, B.R. The Role of In Situ Generated Morphological Motifs and Cu(I) Species in C₂₊ Product Selectivity During CO₂ Pulsed Electroreduction. *Nat. Energy* **2020**, *5*, 317. [[CrossRef](#)]

11. Fan, Q.; Zhang, X.; Ge, X.; Bai, L.; He, D.; Qu, Y.; Kong, C.; Bi, J.; Ding, D.; Cao, Y.; et al. Manipulating Cu Nanoparticle Surface Oxidation States Tunes Catalytic Selectivity toward CH₄ or C₂₊ Products in CO₂ Electroreduction. *Adv. Energy Mater.* **2021**, *11*, 2101424. [[CrossRef](#)]
12. Kim, C.; Cho, K.M.; Park, K.; Kim, J.Y.; Yun, G.T.; Toma, F.M.; Gereige, I.; Jung, H.T. Cu/Cu₂O Interconnected Porous Aerogel Catalyst for Highly Productive Electrosynthesis of Ethanol from CO₂. *Adv. Funct. Mater.* **2021**, *31*, 2102142. [[CrossRef](#)]
13. Wang, J.; Yang, H.; Liu, Q.; Liu, Q.; Li, X.; Lv, X.; Cheng, T.; Wu, H.B. Fastening Br- Ions at Copper-Molecule Interface Enables Highly Efficient Electroreduction of CO₂ to Ethanol. *ACS Energy Lett.* **2021**, *6*, 437. [[CrossRef](#)]
14. Ebaid, M.; Jiang, K.; Zhang, Z.; Drisdell, W.S.; Bell, A.T.; Cooper, J.K. Production of C₂/C₃ Oxygenates from Planar Copper Nitride-Derived Mesoporous Copper via Electrochemical Reduction of CO₂. *Chem. Mater.* **2020**, *32*, 3304. [[CrossRef](#)]
15. Gao, D.; Aran-Ais, R.M.; Jeon, H.; Cuenya, B. Rational Catalyst and Electrolyte Design for CO₂ Electroreduction towards Multicarbon Products. *Nat. Catal.* **2019**, *2*, 198. [[CrossRef](#)]
16. Mosali, V.S.S.; Zhang, X.; Liang, Y.; Li, L.; Puxty, G.; Horne, M.D.; Brajter-Toth, A.; Bond, A.M.; Zhang, J. CdS-Enhanced Ethanol Selectivity in Electrocatalytic CO₂ Reduction at Sulfide-Derived Cu-Cd. *ChemSusChem* **2021**, *14*, 2924. [[CrossRef](#)] [[PubMed](#)]
17. Lei, Q.; Zhu, H.; Song, K.; Wei, N.; Liu, L.; Zhang, D.; Yin, J.; Dong, X.; Yao, K.; Wang, N.; et al. Investigating the Origin of Enhanced C₂₊ Selectivity in Oxide-/Hydroxide-Derived Copper Electrodes during CO₂ Electroreduction. *J. Am. Chem. Soc.* **2020**, *142*, 4213. [[CrossRef](#)]
18. Iyengar, P.; Kolb, M.J.; Pankhurst, J.R.; Calle-Vallejo, F.; Buonsanti, R. Elucidating the Facet-Dependent Selectivity for CO₂ Electroreduction to Ethanol of Cu-Ag Tandem Catalysts. *ACS Catal.* **2021**, *11*, 4456. [[CrossRef](#)]
19. Garza, A.J.; Bell, A.T.; Head-Gordon, M. Mechanism of CO₂ Reduction at Copper Surfaces: Pathways to C₂ Products. *ACS Catal.* **2018**, *8*, 1490. [[CrossRef](#)]
20. Cheng, T.; Xiao, H.; Goddard III, W.A. Reaction Mechanisms for the Electrochemical Reduction of CO₂ to CO and Formate on the Cu(100) Surface at 298 K from Quantum Mechanics Free Energy Calculations with Explicit Water. *J. Am. Chem. Soc.* **2016**, *138*, 13802. [[CrossRef](#)]
21. Zheng, Y.; Vasileff, A.; Zhou, X.; Jiao, Y.; Jaroniec, M.; Qiao, S.Z. Understanding the Roadmap for Electrochemical Reduction of CO₂ to Multi-Carbon Oxygenates and Hydrocarbons on Copper-Based Catalysts. *J. Am. Chem. Soc.* **2019**, *141*, 7646. [[CrossRef](#)] [[PubMed](#)]
22. Montoya, J.H.; Peterson, A.A.; Nørskov, J.K. Insights into C-C Coupling in CO₂ Electroreduction on Copper Electrodes. *ChemCatChem* **2013**, *5*, 737. [[CrossRef](#)]
23. Bai, X.; Li, Q.; Shi, L.; Niu, X.; Ling, C.; Wang, J. Hybrid Cu⁰ and Cu^{x+} as Atomic Interfaces Promote High-Selectivity Conversion of CO₂ to C₂H₅OH at Low Potential. *Small* **2020**, *16*, 1901981. [[CrossRef](#)] [[PubMed](#)]
24. Scholten, F.; Sinev, I.; Bernal, M.; Cuenya, B.R. Plasma-modified Dendritic Cu Catalyst for CO₂ Electroreduction. *ACS Catal.* **2019**, *9*, 5496. [[CrossRef](#)]
25. Xiao, H.; Goddard III, W.A.; Cheng, T.; Liu, Y. Cu Metal Embedded in Oxidized Matrix Catalyst to Promote CO₂ Activation and CO Dimerization for Electrochemical Reduction of CO₂. *Proc. Natl. Acad. Sci. USA* **2017**, *114*, 6685. [[CrossRef](#)]
26. Shang, L.; Lv, X.; Shen, H.; Shao, Z.; Zheng, G. Selective Carbon Dioxide Electroreduction to Ethylene and Ethanol by Core-Shell Copper/Cuprous Oxide. *J. Colloid Interface Sci.* **2019**, *552*, 426. [[CrossRef](#)]
27. Yang, Q.; Liu, X.; Peng, W.; Zhao, Y.; Liu, Z.; Peng, M.; Lu, Y.R.; Chan, T.S.; Xu, X.; Tan, Y. Vanadium Oxide Integrated on Hierarchically Nanoporous Copper for Efficient Electroreduction of CO₂ to Ethanol. *J. Mater. Chem. A* **2021**, *9*, 3044. [[CrossRef](#)]
28. Wu, X.; Fan, H.; Sharif, M.; Yu, Y.; Wei, K.; Zhang, A.; Liu, G. Electrochemically-mediated Amine Regeneration of CO₂ Capture: From Electrochemical Mechanism to Bench-scale Visualization Study. *Appl. Energy* **2021**, *302*, 117553. [[CrossRef](#)]
29. Zhang, L.; Li, M.; Zhang, S.; Cao, X.; Bo, J.; Zhu, X.; Han, J.; Ge, Q.; Wang, H. Promoting Carbon Dioxide Electroreduction Toward Ethanol Through Loading Au Nanoparticles on Hollow Cu₂O Nanospheres. *Catal. Today* **2021**, *365*, 348. [[CrossRef](#)]
30. Liu, P.; Hensen, E.J.M. Highly Efficient and Robust Au/MgCuCr₂O₄ Catalyst for Gas-Phase Oxidation of Ethanol to Acetaldehyde. *J. Am. Chem. Soc.* **2013**, *135*, 14032. [[CrossRef](#)]
31. Platzman, I.; Brener, R.; Haick, R.; Tannenbaum, H. Oxidation of Polycrystalline Copper Thin Films at Ambient Conditions. *J. Phys. Chem. C* **2008**, *112*, 1101. [[CrossRef](#)]
32. Liu, J.; Fu, J.; Zhou, Y.; Zhu, W.; Jiang, L.P.; Lin, Y. Controlled Synthesis of EDTA-Modified Porous Hollow Copper Microspheres for High-Efficiency Conversion of CO₂ to Multicarbon Products. *Nano Lett.* **2020**, *20*, 4823. [[CrossRef](#)] [[PubMed](#)]
33. Ding, L.; Han, Q.; Lu, H.; Yang, Y.; Lu, G.; Zhang, H.; Ran, X.; Xia, Y.; Li, P.; Chen, Y.; et al. Valence Regulation of Ultrathin Cerium Vanadate Nanosheets for Enhanced Photocatalytic CO₂ Reduction to CO. *Catalysts* **2021**, *11*, 1115. [[CrossRef](#)]
34. Kim, J.Y.; Park, W.; Choi, C.; Kim, G.; Cho, K.M.; Lim, J.; Kim, S.J.; Al-Saggaf, A.; Gereige, I.; Lee, H.; et al. High Facets on Nanowrinkled Cu via Chemical Vapor Deposition Graphene Growth for Efficient CO₂ Reduction into Ethanol. *ACS Catal.* **2021**, *11*, 5658. [[CrossRef](#)]
35. Liu, X.; Xiao, J.; Peng, H.; Hong, X.; Chan, K.; Nørskov, J.K. Understanding Trends in Electrochemical Carbon Dioxide Reduction Rates. *Nat. Commun.* **2017**, *8*, 15438. [[CrossRef](#)]
36. Kresse, G.; Furthmüller, J. Efficiency of Ab-Initio Total Energy Calculations for Metals and Semiconductors using a Plane-Wave Basis Set. *Comput. Mater. Sci.* **1996**, *6*, 15. [[CrossRef](#)]
37. Kresse, G.; Furthmüller, J. Efficient Iterative Schemes for Ab Initio Total-Energy Calculations using a Plane-Wave Basis Set. *Phys. Rev. B* **1996**, *54*, 11169. [[CrossRef](#)]

38. Perdew, J.P.; Burke, K.; Ernzerhof, M. Generalized Gradient Approximation Made Simple. *Phys. Rev. Lett.* **1997**, *78*, 1396. [[CrossRef](#)]
39. Kresse, G.; Joubert, D. From Ultrasoft Pseudopotentials to the Projector Augmented-Wave Method. *Phys. Rev. B* **1999**, *59*, 1758. [[CrossRef](#)]
40. Blochl, P.E. Projector Augmented-Wave Method. *Phys. Rev. B* **1994**, *50*, 17953. [[CrossRef](#)]
41. Grimme, S.; Antony, J.; Ehrlich, S.; Krieg, H. A Consistent and Accurate Ab Initio Parametrization of Density Functional Dispersion Correction (DFT-D) for the 94 Elements H-Pu. *J. Chem. Phys.* **2010**, *132*, 154104. [[CrossRef](#)] [[PubMed](#)]